



# Precipitate number density determination in microalloyed steels by complementary atom probe tomography and matrix dissolution

Louis Weber<sup>1</sup>, Johannes Weibel<sup>2,3</sup>, Frank Mücklich<sup>2,3</sup>, and Tobias Kraus<sup>1,4,\*</sup> 

<sup>1</sup>INM–Leibniz Institute for New Materials, Campus D2 2, 66123 Saarbrücken, Germany

<sup>2</sup>Institute for Functional Materials, Saarland University, Campus D3 3, 66123 Saarbrücken, Germany

<sup>3</sup>MECS–Materials Engineering Center Saarland, Campus D3 3, 66123 Saarbrücken, Germany

<sup>4</sup>Colloidal and Interface Chemistry, Saarland University, Campus D2 2, 66123 Saarbrücken, Germany

Received: 9 March 2022

Accepted: 30 May 2022

Published online:

30 June 2022

© The Author(s) 2022

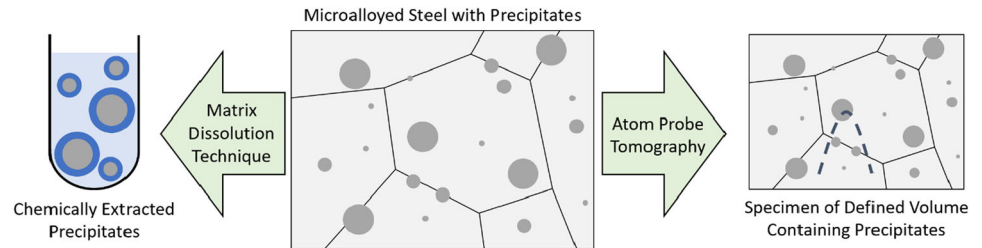
## ABSTRACT

Particle number densities are a crucial parameter in the microstructure engineering of microalloyed steels. We introduce a new method to determine nanoscale precipitate number densities of macroscopic samples that is based on the matrix dissolution technique (MDT) and combine it with atom probe tomography (APT). APT counts precipitates in microscopic samples of niobium and niobium-titanium microalloyed steels. The new method uses MDT combined with analytical ultracentrifugation (AUC) of extracted precipitates, inductively coupled plasma–optical emission spectrometry, and APT. We compare the precipitate number density ranges from APT of 137.81 to 193.56  $\times 10^{21} \text{ m}^{-3}$  for the niobium steel and 104.90 to 129.62  $\times 10^{21} \text{ m}^{-3}$  for the niobium-titanium steel to the values from MDT of 2.08  $\times 10^{21} \text{ m}^{-3}$  and 2.48  $\times 10^{21} \text{ m}^{-3}$ . We find that systematic errors due to undesired particle loss during extraction and statistical uncertainties due to the small APT volumes explain the differences. The size ranges of precipitates that can be detected via APT and AUC are investigated by comparison of the obtained precipitate size distributions with transmission electron microscopy analyses of carbon extraction replicas. The methods provide overlapping resulting ranges. MDT probes very large numbers of small particles but is limited by errors due to particle etching, while APT can detect particles with diameters below 10 nm but is limited by small-number statistics. The combination of APT and MDT provides comprehensive data which allows for an improved understanding of the interrelation between thermo-mechanical controlled processing parameters, precipitate number densities, and resulting mechanical-technological material properties.

Handling Editor: Catalin Croitoru.

Address correspondence to E-mail: tobias.kraus@leibniz-inm.de

## GRAPHICAL ABSTRACT



### Abbreviations

APT	Atom probe tomography
AUC	Analytical ultracentrifugation
CA	Cluster analysis
CER	Carbon extraction replica
DC	Direct current
FIB	Focused ion beam
ICP-OES	Inductively coupled plasma–optical emission spectrometry
ICS	Iso-concentration surfaces
MDT	Matrix dissolution technique
PSD	Precipitate size distribution
SEM	Scanning electron microscope
SR-AUC	Speed ramp analytical ultracentrifugation
TEM	Transmission electron microscopy
TMCP	Thermo-mechanical controlled processing
UPW	Ultrapure water

### Introduction

Microalloyed steels find application in structural part production across numerous industrial sectors such as offshore and pipeline industry or the automotive sector. Their low carbon content ensures good weldability while displaying compelling mechanical properties compared to mild steel. Microalloyed steels contain small amounts (< 0.1 wt%) of niobium, titanium, and/or vanadium [1] which lead to the formation of desirable carbonitride precipitates during thermo-mechanical controlled processing (TMCP). Mechanical-technological properties of

microalloyed steels can be improved by optimization of TMCP parameters such as deformation degree during rolling, or cooling velocities.

In the past, TMCP optimization based on precipitate analysis relied on precipitate size distribution (PSD) and precipitate composition determination at different TMCP stages to monitor precipitation kinetics. Bulk [2–10] and replicated [11–19] samples have widely been investigated to characterize size, shape, and chemical composition of precipitates. The matrix dissolution technique (MDT), where steel samples are dissolved and the remaining precipitates characterized, is currently making its way from microalloyed steel research into industrial application [20, 21]. It provides data that is complementary to the conventional replica routes and can be combined with elemental analysis such as inductively coupled plasma – optical emission spectrometry (ICP-OES) to characterize the chemical composition of particle fractions.

Determining the precipitate number density in microalloyed steels is of great relevance to understand how it affects their mechanical-technological properties and how it can be modified through TMCP. Precipitate number densities cannot be determined via two-dimensional electron microscopy investigations on carbon extraction replicas and/or metallographically prepared cross sections of bulk samples. Further, the small volume fraction of precipitates (below 0.1%) limits the precipitate number density determination to high-resolution tomographic techniques such as X-ray diffraction in synchrotrons [22] or small-angle neutron scattering [5, 23].

Atom probe tomography (APT) has been used to estimate the number density of very small clusters or precipitates in steels at high number densities ( $> 10^{22} \text{ m}^{-3}$ ) where the small investigated volumes of typically around  $10^5 \text{ nm}^3$  contain at least one precipitate [24, 25]. Xie et al. [26] employed APT to investigate age-hardening in a coiled Nb-microalloyed steel and could tie varying cluster size distributions and precipitate number densities to the respective bulk Vickers hardness. Weibel et al. found that NbTi-microalloyed steel precipitates with greatly varying size distributions and number densities can appear simultaneously depending on the TMCP stage investigated [27]. Takahashi et al. investigated Cu precipitates in steel and found that an increase in mean precipitate size was accompanied by a decrease in precipitate number density [25]. The upper limit of APT for statistically robust precipitate number density determination is reached when the mean inter-precipitate distance is close to the dimensions of the APT specimen, typically a few tens to hundreds of nanometers. APT further was used for three-dimensional estimation of precipitate shape by careful inspection and calibration of the atom reconstruction [28, 29].

Precipitate number densities from MDT have not been reported in the literature to the best of our knowledge. MDT has been successfully applied to obtain distributions of precipitate size, shape, and chemical composition [20, 21], where it probes a much larger sample volume (several tens of  $\text{mm}^3$ ) than APT or replica techniques. Hegetschweiler et al. [30] report that an improved extraction protocol enables the analysis of sub-10 nm precipitates extracted from a NbTi-microalloyed steel.

Here, we combine MDT with AUC analysis of chemically extracted precipitates and APT to reconstruct their average number density in macroscopic sample volumes. Unlike APT the combination of MDT and AUC relies on indirect precipitate characterization. AUC is a fractionating characterization technique enabling analysis of colloidal systems [31–33]. Optical extinction of sedimenting precipitates is acquired to obtain a sedimentation coefficient distribution from which an extinction weighted PSD can be calculated. A Mie correction [34] is then applied to the extinction weighted PSD to determine a mass weighted PSD, prior to determination of a number weighted PSD. Number weighted PSDs are

determined with Ångstrom resolution and high statistical significance in AUC [35].

In this contribution, number densities of NbC and NbTiCN precipitates in model Nb and NbTi-microalloyed steels were determined via APT and MDT. The discrepancies in precipitate number densities provided by the two techniques are discussed in view of the very different probed volumes. The validity of the standard assumptions on complete precipitation, sample homogeneity, and the resolving power of APT and AUC across different precipitate size ranges are discussed. We combined APT and MDT to cover a large precipitate number density range and to provide a holistic picture of the precipitate distribution in microalloyed steels.

## Experimental procedures

### Materials

Two high-Nb microalloyed low-carbon steels were obtained from Comtes FHT, Dobřany, Czech Republic, one containing titanium (“Steel NbTi” in the following), one without (“Steel Nb”). The elemental compositions as measured by the AG der Dillinger Hüttenwerke, Dillingen/Saar, Germany, with pulse discrimination analysis–optical emission spectrometry are given in Table 1. The concentration values are average values from measurements on three cross sections along the length of the cast

**Table 1** Elemental composition of the investigated microalloyed steels

Element	Steel Nb (wt%)	Steel NbTi (wt%)
C	0.04	0.04
Si	0.32	0.33
Mn	1.69	1.70
N	0.004	0.006
Cu	0.22	0.22
Ni	0.23	0.20
Mo	0.02	0.02
Cr	0.05	0.04
V	0.001	0.001
Nb	0.082	0.085
Ti	0.001	0.018
CEV <sup>1</sup>	0.36	0.36

<sup>1</sup>Carbon-equivalent value

blocks, each with nine measuring points (27 in total). The standard deviations across multiple measurements of the measured concentrations were below 0.002 wt% for most elements, indicating highly accurate measurements. Larger uncertainties occurred for a few samples and for some elements at higher concentrations such as Si, C, Mn, and Al; their standard deviations were around 0.005 wt%, but always below 0.01 wt%. Steel Nb was heat treated at AG der Dillinger Hüttenwerke (1000 °C for 1 h) to dissolve the cast structure and completely precipitate niobium. Steel Nb was then processed to ensure that all alloyed niobium forms fine NbC precipitates at a high number density. To this end, a  $2 \times 2 \times 2 \text{ cm}^3$  Nb steel volume was heated to 1250 °C for 30 min to ensure complete precipitate dissolution, quenched in water, heated to 690 °C, and kept there for 60 min to allow for complete precipitation of NbC, upon which the sample was again quenched in water. Thermal treatment was carried out in a furnace model HT 04/17 (Nabertherm, Lilienthal, Germany) in air. 5 mm of oxidized and decarburized material were mechanically removed from each side of the sample prior to chipping samples for characterization. The sample was selected because it is known to contain fine and homogeneous NbC.

Steel NbTi was slowly cooled after casting of a 500 kg ingot. During transformation from austenite to ferrite, fine interphase precipitation occurred because the solubility of Nb is much lower in ferrite than in austenite [36]. A fraction of Ti precipitated at higher temperatures to form larger cubic and insoluble TiN [37]. The sample was selected because it contains a broad size distribution of precipitates for the evaluation of the used methods and also a high precipitation density of fine NbTiCN.

## Characterization methods

### *Atom probe tomography (APT)*

APT was carried out in a LEAP 3000XHR (Cameca SAS, Gennevilliers, France). Specimens were cooled down to 60 K in an ultra-high vacuum ( $1.33 \times 10^{-8}$  Pa). A direct current (DC) bias of up to 11 kV induced field-evaporation of single atoms toward a local electrode in front of a multi-plate detector. Upon reaching the bias threshold for field-evaporation, the voltage pulsed at 200 kHz with 15% of the DC bias to allow for controlled evaporation of

ionized atoms. The DC bias was constantly adjusted to limit the detector signal to 3 ions per 1 000 pulses. The commercial software package IVAS 3.6.14 (Cameca SAS, Gennevilliers, France) was used for analysis of the detected ions. Atom positions in three-dimensional space were reconstructed based on crystallographic information that we applied to deconvolute the detector hit map [29]. Crystallographic poles were identified, and the map was fit with a model with tip radius and image compression factor as fitting parameters. The parameters were adjusted until the reconstructed Fe atoms had the known interplanar distance of iron for the respective crystallographic poles.

Apparent precipitate sizes ranged from 1 to 20 nm. Both iso-concentration surfaces (voxelization of  $1 \times 1 \times 1 \text{ nm}^3$  and a delocalization of  $3 \times 3 \times 1.5 \text{ nm}^3$  in  $x$ ,  $y$ , and  $z$  direction, respectively) and a cluster-algorithm implemented in the software IVAS were applied to delineate precipitates. Reconstructed precipitates are likely magnified due to their comparably higher evaporation field strength [38]. We estimated the true diameters by the size of the void of reconstructed Fe atoms (indicated by low Fe atom density in the region of precipitates) rather than the precipitate elements themselves, following the approach of Breen et al. [28]. Nb iso-concentration values were chosen according to those Fe low-density regions. They ranged from 1 at% Nb for very small to around 3 at% for the largest Nb-precipitates. Alternatively, the cluster-detection algorithm implemented in IVAS was used [39]. Relatively high values were chosen for the maximum distance between two atoms belonging to the same cluster,  $D_{\text{max}}$ , the envelope parameter  $L$  and the erosion distance parameter  $E$ . The values for  $D_{\text{max}}$  and  $L$  were set to 2 nm and  $E$  to 1 nm. The minimum number of atoms defining a cluster ( $N_{\text{min}}$ ) was set to 4 atoms. Four Nb atoms needed to be within  $D_{\text{max}}$  of each other to be attributed to the cluster to exclude random fluctuations of Nb atoms. The results were used to estimate a range for the true precipitate number densities.

### *Analytical ultracentrifugation (AUC)*

A multiwavelength analytical ultracentrifuge was built using the design of the open AUC project on the basis of a preparative ultracentrifuge type Optima XL-80 K (Beckman Coulter, Brea, USA) [40]. Measurement cells with 12 mm titanium centerpieces

were employed. Speed ramp AUC (SR-AUC) data were acquired between 1 and 50 kRPM (30 min at maximum speed) at 20 °C with a radial position of 6.7 cm at a wavelength of 450 nm. The measured data were evaluated using the freely available software HDR-Multifit [41, 42] before applying a Mie correction [43, 44] and determining a number weighted PSD with the free scientific python development environment Spyder (version 3.2.6) included with Anaconda. The code for Mie correction and PSD determination was introduced in previous work by Hegetschweiler [45]. The refractive index of NbC was set to  $2.07 + 2.25i$ , that of NbTiCN to  $1.72 + 1.55i$ . The NbC density was  $7820 \text{ kg.m}^{-3}$ , that of NbTiCN to  $6655 \text{ kg.m}^{-3}$ . The Disperbyk-2012 density was set to  $1056 \text{ kg.m}^{-3}$  and the ligand shell thickness to 5.7 nm [45].

#### *Inductively coupled plasma–optical emission spectrometry (ICP-OES)*

ICP-OES analysis of steel chippings was carried out with a Jobin Yvon Ultima 2 instrument (Horiba, Kyoto, Japan) equipped with a PEEK MiraMist nebulizer (PerkinElmer Inc., Waltham, USA) at 3.00 bar and  $0.71 \text{ L.min}^{-1}$ . Niobium was detected at an emission wavelength of 313.079 nm and titanium at 337.280 nm.

#### *Transmission electron microscopy (TEM)*

Precipitate analysis was carried out with a JEM-2100(HR) transmission electron microscope (JEOL, Akishima, Japan) equipped with a LaB<sub>6</sub> electron source at 200 kV. Precipitates were imaged with an Orius Model 832 camera (Gatan Inc., Pleasanton, USA).

### **Sample preparation**

#### *APT specimen preparation*

The bulk samples were analyzed by APT at random sample positions across the polished steel surface. The samples were ground with SiC grinding paper up to 1200 mesh grid, polished on cloth disks with diamond suspension using decreasing particle sizes (6,3, and 1  $\mu\text{m}$ ), and finally oxide polished with a 0.05  $\mu\text{m}$  silica particle suspension. Specimens were cut in a focused ion beam equipped scanning electron

microscope (FIB-SEM) model Helios Nanolab™ 600 (Thermo Fisher Inc., Waltham, USA, formerly FEI Company, Hillsboro, USA) following the standard FIB lift-out method [46]. The lift-out bar was transferred to a multi-tip array of pre-fabricated Si posts and fixated with electrodeposited Pt. FIB annular milling with 30 kV and a 5 kV step for final sharpening produced specimen tips with a tip radius below 50 nm. APT specimen tips were imaged in FIB before and after field evaporation to compare the dimensions of probed material volume with the reconstructed tip volume that was adjusted to the crystallographic information extracted from the detector hit map.

#### *Precipitate extraction for AUC*

All chemicals were used as purchased without any further purification. Ultrapure water (UPW) was produced in a Milli-Q water-purification system (Advantage A10 and Elix 20, Millipore Corporation, Burlington, USA). 500 mg of steel chippings were dissolved in a 25 mL etching solution composed of  $0.5 \text{ mol.L}^{-1} \text{ H}_2\text{SO}_4$  prepared from conc.  $\text{H}_2\text{SO}_4$  (95–97%, p.a., Sigma-Aldrich, Germany) by dilution with UPW and 0.1 vol.% Disperbyk-2012 (BYK Additives & Instruments, Wesel, Germany) at 70 °C following the extraction protocol developed by Hegetschweiler et al. [30] The reaction mixture was stirred at 200 RPM until dissolution completion and sonicated for 15 min in an ultrasonic bath type Sonorex Super RK 514 BH (BANDELIN electronic GmbH & Co. KG, Berlin, Germany). Suspension purification was carried out with a preparative ultracentrifuge type Optima XE-90 (Beckman Coulter, Brea, USA) at 504 300 RCF at 20 °C for 90 min. The suspension was centrifuged eight times. Purification was carried out by supernatant removal, residue redispersion via sonication, and supernatant replacement with fresh UPW after each centrifugation run. Completion of the eighth centrifugation step, supernatant removal, and residue redispersion via sonication led to a precipitate suspension of approximately 5 mL.

#### *Sample dissolution for ICP-OES*

A mixture of 25 mL HCl ( $\geq 37\%$ , p.a. puriss, Sigma-Aldrich, Germany), 8 mL  $\text{HNO}_3$  ( $\geq 65\%$ , p.a. puriss, Sigma-Aldrich, Germany), and 17 mL UPW was

prepared. 5 mL of this acid mixture was combined with 1 mL of HF (50%, p.a. plus, Riedel-de-Haën, Germany) and used to etch 22.14 mg of Steel Nb chippings or 21.28 mg of Steel NbTi chippings in Teflon microwave vessels. The reaction mixture was irradiated with microwaves using a 0–800 W ramp in 1 h and constant 800 W for 1 h 30 min for Steel Nb. Steel NbTi was exposed to 0–600 W ramp in 1 h and a constant 600 W for 1 h 30 min. After cooling, the solutions were transferred to 50 mL flasks and filled up to the calibration marks with UPW prior to analysis.

### Carbon extraction replica preparation

Carbon extraction replicas were prepared from steels Nb and NbTi. Polished steel surfaces (prepared analogously to the APT surfaces) were etched with 3 vol% alcoholic nitric acid (65% Suprapur®, Merck, Darmstadt, Germany) for 30 s, and a layer of carbon was deposited (K950X Turbo Evaporator, Emitech, now Quorumtech, Laughton, UK). The film was incised with a scalpel to form squares with 3 mm length and the sample was immersed into the acid solution for up to 30 min. Delaminated C-films were captured by 200 mesh TEM-grade copper grids and rinsed in a mixture of 30:70 ethanol and water prior to air drying.

### APT measurement error estimation and statistical uncertainty determination

Measurement errors in precipitate number densities from APT are mainly due to incorrectly identified precipitates. The value from iso-concentration surfaces provides a lower limit and cluster analysis an upper limit for the true number of precipitates inside the APT volume. Precipitates located at specimen-edges were counted as 0.5 particles following the planimetric procedure approach [47].

The statistical uncertainty in average particle density was determined assuming a Poisson distribution for the number of precipitates per specimen (Eq. 1). If  $\lambda \in \mathbb{R}_+$  and  $X$  is a real random variable.  $X$  follows Poisson's law of parameter  $\lambda$  and  $X \rightarrow P(\lambda)$  if:

$$X(\Omega) = \mathbb{N} \text{ and } \forall n \in \mathbb{N}, P(X = n) = e^{-\lambda} \cdot \frac{\lambda^n}{n!} \quad (1)$$

We determined the 95% probability range for the number of particles per investigated steel volume

and precipitate identification technique based on the average precipitates per specimen. This range was converted to a precipitate number density range using the average specimen volume.

### MDT measurement error estimation

We considered the random errors of the precipitate diameters and Nb/Ti concentrations. AUC analysis provides precipitate diameters at Ångström resolution [48] with a diameter measurement error of approximately 1%. ICP-OES analysis provides the niobium content with a measurement error of 1.7% for Steel Nb and 2.5% for Steel NbTi and the titanium content with a measurement error of 3.5% for Steel NbTi. We obtained these measurement errors by comparing the ICP-OES results (with errors that are typically below 0.1%) to the values listed in Table 1. We estimate the compound measurement error in precipitate number density from MDT to be approximately 5% for Steel Nb and 6% for Steel NbTi.

## Results

### Precipitate characterization via APT

Reconstructed atom maps of Steel Nb and NbTi are displayed in Fig. 1a, b. From the detector hit maps of all APT experiments, the crystallographic information, as is exemplarily shown in Fig. 1c, was used to calibrate the atom reconstructions [29]. Approximately 50 and 100 particles were identified in total, respectively, and their chemical compositions were determined. We found that the Nb:C atomic ratios varied from 42:58 to 55:45 and concluded that precipitates in Steel Nb (Fig. 1a) contain Nb and C in equal atomic fractions to form NbC. Note that NbC<sub>1-x</sub> precipitates have been reported, too [49]. Precipitates in Steel NbTi (Fig. 1b) had the average composition Nb<sub>0.76</sub>Ti<sub>0.24</sub>C<sub>0.89</sub>N<sub>0.11</sub> (Nb<sub>x</sub>Ti<sub>1-x</sub>C<sub>y</sub>N<sub>1-y</sub>). As with NbC in Steel Nb, metal and non-metal atoms were in near 1:1 atomic ratio. Nb precipitates were oblate, almost disk-shaped, whereas those in Steel NbTi were almost ideal spheres.

In Steel Nb, we mostly observed ellipsoid precipitates with a size of approximately 5 nm in the long axis and only 1–2 nm in the short axis. The crystal orientation from crystal pole analysis in APT indicated that the Nb-precipitates had their (100) habit

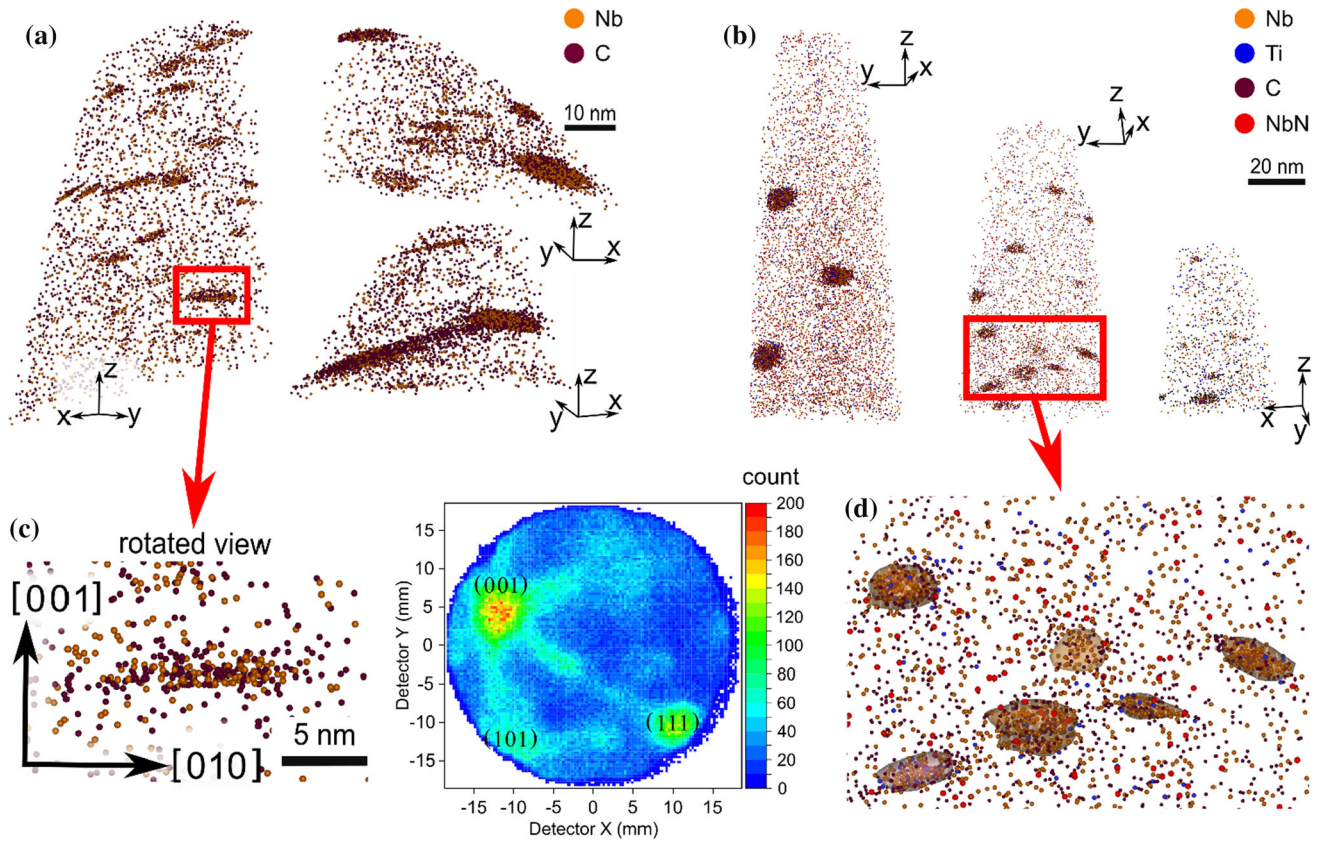


**Figure 1** Reconstructed atom maps of several specimens of **a** Steel Nb showing Nb and C atoms and **b** Steel NbTi showing Nb, Ti, C, and N (from NbN peak) atoms. **c** Magnified rotated view from the reconstruction in the red frame in **a**) showing an oblate precipitate which lies on the (001) plane. The orientation

planes oriented along the [100] or [010] direction (Fig. 1c). We also observed relatively larger precipitates reaching 15–20 nm in the long axis which were situated on C-decorated defects (lower right image of Fig. 1a). Precipitates in Steel NbTi, as exemplarily shown in Fig. 1b and d, have a near spherical shape in contrast to the oblate shape in Fig. 1a, c.

We calculated precipitate number densities by counting the precipitates in specimens of known volumes. The mean density in Steel Nb (Table 2) from iso-concentration surfaces (ICS) was  $137.81 \times 10^{21} \text{ m}^{-3}$ ; cluster analysis (CA) indicated  $193.56 \times 10^{21} \text{ m}^{-3}$ . Assuming uniform densities throughout the sample, Student’s t analysis was used to estimate the errors of the means as 27.68 and  $43.70 \times 10^{21} \text{ m}^{-3}$ . Steel NbTi (Table 3) had mean densities of  $104.90 \times 10^{21} \text{ m}^{-3}$  and  $129.62 \times 10^{21} \text{ m}^{-3}$  for the two analysis methods with estimated errors of 39.52 and  $57.40 \times 10^{21} \text{ m}^{-3}$ . Cluster analysis

was deduced from the crystal poles visible on the detector hit map (multiple detection events shown only). **d** Magnified view of red-framed proportion of reconstruction in **b**) with 1 at% iso-concentration surface of Nb overlaid.

consistently yielded higher values. The difference between the densities returned by both methods is larger for Steel Nb which had mostly smaller and plate like precipitates, whereas Steel NbTi had spherical particles which were more robustly detected with the iso-concentration method.

### Precipitate number density determination via MDT

Chemically extracted precipitates were analyzed via AUC to determine an average precipitate mass (Eq. 2) and via ICP-OES to provide the total niobium and titanium masses.

$$m_{\text{precipitate}} = \rho_{\text{core}} * \frac{4}{3} * \pi * r^3 \tag{2}$$

with  $m_{\text{precipitate}}$  the average precipitate mass,  $\rho_{\text{core}}$  the density of NbC ( $7820 \text{ kg.m}^{-3}$ ) or NbTiCN ( $6655 \text{ kg.m}^{-3}$ ), and  $r$  the precipitate radius. The

**Table 2** APT precipitate number density in Steel Nb

Specimen		Iso-concentration surfaces		Cluster analysis	
Number	Volume (nm <sup>3</sup> )	Precipitate count	Density (10 <sup>21</sup> m <sup>-3</sup> )	Precipitate count	Density (10 <sup>21</sup> m <sup>-3</sup> )
1	48 700	8 + 3 × 0.5 = 9.5	195.07	13 + 4 × 0.5 = 15.0	308.01
2	75 500	4 + 2 × 0.5 = 5.0	66.23	8 + 2 × 0.5 = 9.0	119.21
3	140 100	17 + 7 × 0.5 = 20.5	146.32	25 + 7 × 0.5 = 28.5	203.43
4	38 300	5 + 1 × 0.5 = 5.5	143.60	5 + 1 × 0.5 = 5.5	143.60
Mean			137.81	193.56	
Student Error			27.68	43.70	

**Table 3** APT precipitate number density in Steel NbTi

Specimen		Iso-concentration surfaces		Cluster analysis	
Number	Volume (nm <sup>3</sup> )	Precipitate count	Density (10 <sup>21</sup> m <sup>-3</sup> )	Precipitate count	Density (10 <sup>21</sup> m <sup>-3</sup> )
5	148 400	3 + 1 × 0.5 = 3.5	23.58	4 + 1 × 0.5 = 4.5	30.32
6	49 200	7 + 3 × 0.5 = 8.5	172.76	7 + 3 × 0.5 = 8.5	172.76
7	153 000	34 + 11 × 0.5 = 39.5	258.17	54 + 14 × 0.5 = 61	398.69
8	49 200	6 + 3 × 0.5 = 7.5	152.44	7 + 3 × 0.5 = 8.5	172.76
9	182 600	3 + 2 × 0.5 = 4.0	21.91	4 + 2 × 0.5 = 5.0	27.38
10	150 200	12 + 5 × 0.5 = 14.5	96.54	12 + 5 × 0.5 = 14.5	96.54
11	112 300	1 + 0 × 0.5 = 1.0	8.90	1 + 0 × 0.5 = 1.0	8.90
Mean			104.90	129.62	
Student Error			39.52	57.40	

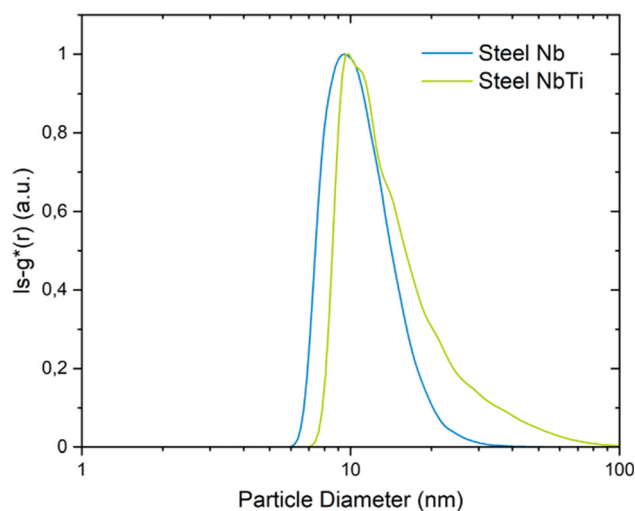
ligand shell contribution to the precipitate mass was neglected.

The calculation of densities (Eq. 3) requires the total carbon and/or nitrogen masses contained in precipitates.

$$\frac{m_{\text{Nb}} + m_{\text{Ti}} + m_{\text{C}} + m_{\text{N}}}{m_{\text{precipitate}}} * \frac{\rho_{\text{steel}}}{m_{\text{dissolved steel}}} = \text{precipitates per m}^3 \quad (3)$$

with  $m_{\text{X}}$  the total mass of an element X contained in the precipitates,  $\rho_{\text{steel}}$  the steel density (7860 kg.m<sup>-3</sup>), and  $m_{\text{dissolved steel}}$  the mass of chemically dissolved steel.

For Steel Nb, we first assumed an Nb:C stoichiometry of 1:1 as reported in the literature [50] to determine the carbon mass and verified the assumption using our APT results. The carbon and nitrogen fractions for Steel NbTi were directly taken from the APT results. Alternatively, extraction replicas with Al<sub>x</sub>O<sub>y</sub> or Al films can be used to investigate the carbon to nitrogen ratio in precipitates. The

**Figure 2** Number weighted PSDs determined via SR-AUC for Steel Nb and Steel NbTi.

suspension obtained by dissolving Steel Nb was analyzed via SR-AUC to determine a number weighted PSD. We found a monomodal size

distribution (Fig. 2) with a modal precipitate diameter of 9.5 nm that corresponds to an average precipitate mass (Eq. 2) of  $3.51 \times 10^{-15}$  mg. The bulk Nb content of the steel from ICP-OES was 0.0821 wt% (Table 4), indicating a niobium mass of 0.42 mg in the steel chippings that we dissolved. The carbon mass of 0.05 mg was determined from the niobium mass by assuming a Nb:C stoichiometry of 1:1 [50] which is in accordance to APT results. A precipitate number density of  $2.08 \times 10^{21} \text{ m}^{-3}$  with a measurement error of  $0.10 \times 10^{21} \text{ m}^{-3}$  was determined for Steel Nb using Eq. 3.

The suspension obtained by dissolving Steel NbTi was analyzed via SR-AUC to determine a number weighted PSD. We found a monomodal precipitate population (Fig. 2) with a modal precipitate diameter of 10.2 nm that implied an average precipitate mass (Eq. 2) of  $3.70 \times 10^{-15}$  mg. The bulk Nb and Ti contents of the steel from ICP-OES were 0.0811 wt% and 0.0227 wt%, respectively (Table 4) equivalent to a niobium mass of 0.41 mg and a titanium mass of 0.11 mg contained in the steel chipping mass dissolved for AUC analysis. According to APT the carbon mass corresponds to 10% of the precipitate mass and the nitrogen mass to 1% of the precipitate mass. A precipitate number density of  $2.48 \times 10^{21} \text{ m}^{-3}$  with a measurement error of  $0.15 \times 10^{21} \text{ m}^{-3}$  was determined for Steel NbTi using Eq. 3.

## Discussion

The precipitate number densities determined via APT and MDT for Steel Nb and NbTi (Table 5) were in the range expected from previously published findings [5, 24]. There was a large discrepancy between the values found by the different methods (Fig. 3). First, we discuss whether MDT analysis correctly assumes that all Nb (and Ti) precipitates,

because solid solutions would falsify the results. Second, we discuss the sample homogeneity and possible effects of heterogeneity on the two methods.

## Degree of Nb/Ti precipitation

The ICP-OES step after MDT does not differentiate between matrix and precipitate contributions. Residual dissolved Nb/Ti therefore directly translates into measurement errors and overestimated precipitate number densities. Metallurgical models let us estimate the magnitude of this error. Perrard et al. [23] established a time temperature transformation diagram for a very similar high-niobium alloy via small-angle neutron scattering. According to their data precipitation kinetics are above 90% completed. In the present work, the APT analysis of Steel Nb corroborated these results as less than 0.002 wt% Nb was measured inside the precipitate- or cluster-free matrix, equivalent to 97.5% precipitation of nominal Nb. Steel matrix of Steel NbTi also was practically depleted of all Nb (0.001 wt% Nb in solution) which is reasonable when considering the slow cooling of the ingot and the low solubility of Nb in ferrite.

## Sample homogeneity

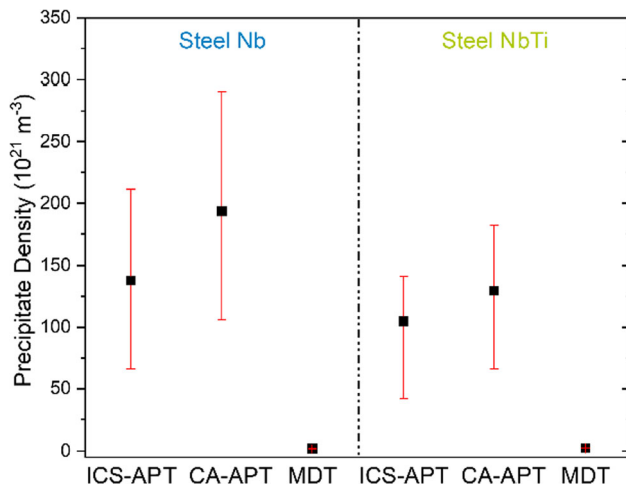
The microalloyed steel samples were chosen for homogeneity to enable a comparison of the 100 nm-scale APT with the mm-scale MDT analysis. Commercial steel samples are homogenous at the mm scale, with the possible exception of steels with center-line segregation precipitation. Analysis on the 100 nm scale, in contrast, is sensitive to the sampling position with respect to grain boundaries. We must consider whether the Nb distribution at the 100 nm scale found with APT can be compared to the millimeter-scale results from MDT.

**Table 4** ICP-OES analysis results for Steel Nb and Steel NbTi

	Steel Nb	Steel NbTi	
	Nb	Ti	Nb
Sample Content ( $\text{mg.L}^{-1}$ )	$0.3635 \pm 0.0061$	$0.0963 \pm 0.0012$	$0.3451 \pm 0.0090$
Limit of Detection ( $\mu\text{g.L}^{-1}$ )	1.2	1.1	1.3
Limit of Quantification ( $\mu\text{g.L}^{-1}$ )	4.1	3.7	4.3
Mass Fraction (wt%)	$0.0821 \pm 0.0014$	$0.0227 \pm 0.0008$	$0.0811 \pm 0.0020$

**Table 5** Precipitate number densities and measurement errors as determined via APT and MDT

Technique	Steel sample	Precipitates per m <sup>3</sup> ( $\times 10^{21}$ )	Investigated steel volume (m <sup>3</sup> )
APT	Steel Nb	137.81 $\pm$ 27.68 to 193.56 $\pm$ 43.70	3.0 $\times 10^{-22}$
	Steel NbTi	104.90 $\pm$ 39.52 to 129.62 $\pm$ 57.40	8.4 $\times 10^{-22}$
MDT	Steel Nb	2.08 $\pm$ 0.10	6.5 $\times 10^{-8}$
	Steel NbTi	2.48 $\pm$ 0.15	6.3 $\times 10^{-8}$

**Figure 3** Precipitate number densities for Steel Nb and NbTi with the statistical uncertainties for APT and the measurement errors for MDT.

Micro-segregation during melt solidification is known to change the Nb solute concentrations between dendritic and inter-dendritic regions by a factor of up to 1.6 at a length scale of hundreds of microns [51]. The homogenization treatment at 1250 °C of Steel Nb probably removed such heterogeneities. Steel NbTi did not undergo such a treatment, but APT results from Steel NbTi indicated less heterogeneity than Steel Nb and indicated that other alloying elements that do not precipitate (e.g., Si, Cu, and Ni) were evenly distributed. Nb has a comparatively large diffusivity and should be equally homogenous in spatial distribution. The standard error of APT precipitate density is therefore not influenced by chemical homogeneity of the sample material.

Defect structures may affect precipitate distribution, too. Steel Nb was isothermally held after a martensitic transformation and had a fine lath structure that is visible in carbon extraction replica and has a high grain boundary density. The lower right APT reconstruction in Fig. 1a illustrates that precipitates in the vicinity of the C-decorated martensite laths are much larger [52]. This can be explained by

faster pipe-diffusion along such defects that enhanced nucleation and growth [53]. Steel NbTi had its microstructure transformed from austenite to ferrite during slow cooling and therefore fewer defects that interfere with the precipitation. This may contribute to the slightly higher uncertainties in the APT precipitate density in Steel Nb compared to Steel NbTi.

All APT measurements consistently indicated the presence of precipitates despite the small probed volume. We conclude that the samples of the steels studied here were sufficiently homogeneous for APT to give reasonable precipitate number density values. Even the lowest precipitate density found ( $8.90 \times 10^{21} \text{ m}^{-3}$ , Table 3) in APT was 4 times above that from MDT, with an uncertainty that is mainly due to the small probed sample volume and small number of APT measurements.

### Minimum Detectable Precipitate Sizes

The measurement errors of MDT depicted in Fig. 3 do not consider possible particle etching and loss [30] during chemical extraction that can bias the size distribution toward smaller diameters. Particles below a certain diameter can be etched during extraction and shrink, and smaller particles may be entirely consumed. Etching leads to an underestimated precipitate mass and an overestimated particle number density, complete dissolution of the smallest precipitates leads to the opposite. We compared APT and MDT results to find the minimum precipitate diameters that can be detected via AUC after MDT. Precipitate size distributions (PSDs) were calculated from the APT datasets using the method of Breen et al. [28] and converted to volume-equivalent sphere diameters that we use in the following. We found that AUC did not detect precipitates with diameters below 6 nm for Steel Nb and below 7 nm for Steel NbTi although APT indicated their presence (Fig. 4). The true precipitate diameter might be smaller than reconstructed by APT. Apparent precipitate size and

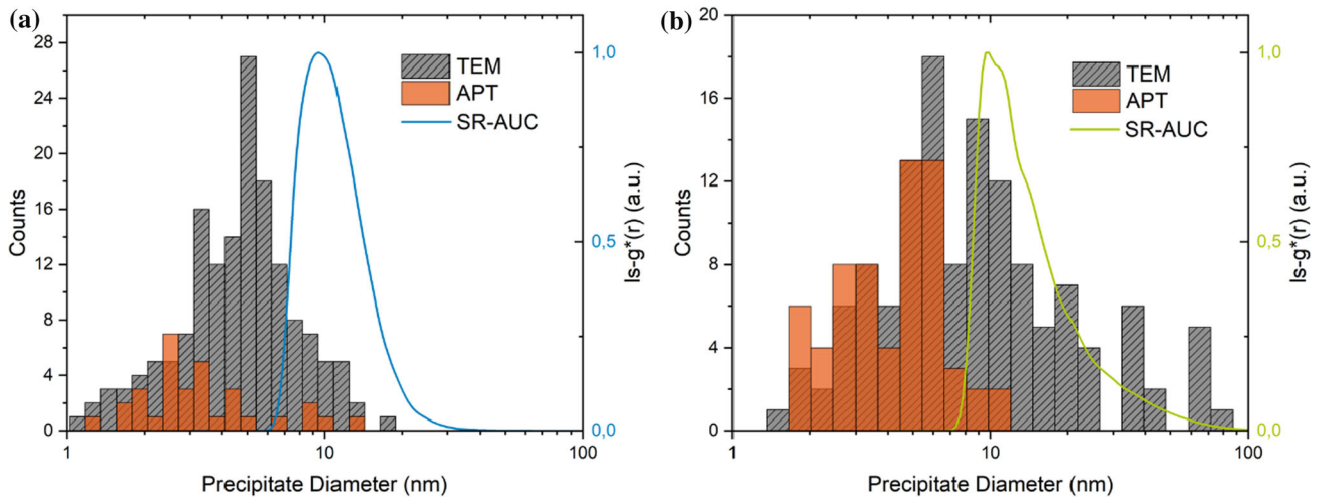


**Figure 4** Number weighted PSDs determined via AUC and APT for **a** Steel Nb and **b** Steel NbTi.

shapes can be affected by the so-called local magnification that is caused by different evaporation field strengths of adjacent phases [38]. The Nb precipitates cause a higher field strength than iron [54] and their shape will be somewhat distorted, but the large difference in precipitate morphology between both steels indicates that rather the particle nucleation and growth is the reason for the morphology differences [26]. The high solution temperature used for Steel Nb, quenching and successive aging at 690 °C caused Nb precipitation from a highly supersaturated ferrite matrix that has a low solubility for Nb. The driving force for nucleation is large and results in finely dispersed precipitates; the mismatch of ferrite and NbC lattices favors the formation of precipitates over the formation path of Guinier–Preston zones [28, 55]. We additionally performed a TEM analysis of carbon extraction replicas (CERs) of both steels and compared the results to our MDT-AUC data. There was a clear offset between PSDs from TEM and AUC that we attribute to complete dissolution of the smallest precipitates and etching of all precipitates. The oblate precipitate shape in Steel Nb (Fig. 1) may aggravate etching. We conclude that MDT underestimates the true precipitate number density because of particle loss and estimated the resulting error in the particle number density by using modal diameters from CERs, which indicate particle densities of  $14.26 \times 10^{21} \text{ m}^{-3}$  for Steel Nb and of  $12.20 \times 10^{21} \text{ m}^{-3}$  for Steel NbTi, one order of magnitude above AUC-based data. A concurrent precipitate diameter reduction of approximately 5% [30]

through undesired etching leads to a slightly underestimated precipitate mass and overestimated precipitate number density. Adding 5% to all precipitate diameters would imply densities of  $1.80 \times 10^{21} \text{ m}^{-3}$  for Steel Nb and of  $2.15 \times 10^{21} \text{ m}^{-3}$  for Steel NbTi. This implies that particle loss biases the precipitate number density from MDT more strongly than particle etching for the investigated microalloyed steels.

The minimum particle size detectable by APT is set by the detection efficiency (37% in the used machine). Clusters consisting of only a few atoms cannot be distinguished from solutes. The maximum particle size detectable by APT is set by the reconstructed volume. Particles which were not completely contained in the specimen were accounted for as half a particle. Particle densities from the iso-concentration method were consistently below that from cluster analysis. The cluster algorithm indicated a practically Nb-free steel matrix (0.001 to 0.002 at%), which implies that all Nb was detected as precipitate components and yielded an upper limit for the precipitate density. Some of the detected “clusters” may merely be groups of  $N_{\min} = 4$  or more Nb atoms in solid solution that are close enough to appear as a cluster, which is possible due to the comparatively larger values for  $D_{\max}$  and L chosen in this study. The cluster algorithm thus probably overestimates the precipitate number density. The iso-concentration method is based on a (manual) visual inspection of images at different Nb iso-concentrations that are chosen such that all atoms that belong to precipitates are enveloped. A lower iso-concentration value

reduces the fraction of atoms in solution that are mistaken for precipitated but increases the risk of missing precipitates. The lower limit for a feasible iso-concentration value depends on experimental factors including the local magnification caused by the difference in evaporation field strength required for carbonitrides and the Fe matrix [38]. The local magnification decreased the Nb concentration gradient at the precipitate-matrix interface. It is affected by particle geometry, too: The difference in precipitate number densities from cluster analysis and iso-concentration surfaces was larger for Steel Nb that contained oblate precipitates with a thickness down to a few atoms. Both evaporation field strength differences and oblate shapes lead the iso-concentration method to miss very small precipitates. The true precipitate number density therefore lies between the values determined via cluster analysis and iso-concentration surfaces.

Disregarding partial precipitates did not much change the results and led to densities of 117.29 to  $170.47 \times 10^{21} \text{ m}^{-3}$  for Steel Nb and of 87.41 to  $110.74 \times 10^{21} \text{ m}^{-3}$  for Steel NbTi. The result for Steel NbTi is on the same order as the values found by MDT after particle loss correction; the result for Steel Nb that contains smaller precipitates is one order of magnitude larger.

In summary, MDT provides a lower limit for the particle number density, while APT yields an upper limit. The main limitation of MDT is undesired particle loss, while APT is limited in the probed volume. Together, the methods provide a reliable range that is not available on other routes and consistent with metallurgical predictions.

## Conclusions

We determined precipitate number densities of two microalloyed steels via APT and a novel technique based on MDT. The MDT precipitate number density determination technique relied on AUC analysis of chemically extracted precipitates and ICP-OES analysis of bulk steel chippings. We find that MDT provides a lower limit and APT an upper limit, because particle etching during chemical extraction affects the precipitate analysis in MDT and the small accessible volume limits APT. MDT and APT were found to be complementary in terms of accessible precipitate size ranges, chemical precipitate composition

information, and precipitate morphology. Further reduction in undesired precipitate etching and loss, e.g., via electrolytic extraction, would benefit precipitate number density determination accuracy.

The MDT-APT combination can be used to analyze all TMCP steps. We are confident that the ability to determine precipitate number densities in all these process steps will lead to an improved understanding of the interrelation between processing parameters and mechanical-technological properties. Further development is required to cover TMCP steps with incomplete precipitation, where combinations of APT and MDT can potentially provide useful information. A holistic picture of the entire process will require the combination of APT and MDT with resistivity measurements and simulations.

## Acknowledgements

The authors would like to thank Andrea Jung for ICP-OES analysis and Dr. Johannes Walter for guidance in SR-AUC implementation.

## Funding

Open Access funding enabled and organized by Projekt DEAL. L.W. and T.K. express their gratitude to the Aktien-Gesellschaft der Dillinger Hüttenwerke, Dillingen/Saar, Germany, for providing the financial funding of this work. J.W. and F.M. express their gratitude to Companhia Brasileira de Metalurgia e Mineracao (CBMM) for providing the financial funding of this work. Furthermore, J.W. and F.M. would like to thank the Saarland State Chancellery for financial support within the ZuMat Project funded by the European Regional Development Fund (ERDF). The Atom Probe was financed by the Deutsche Forschungsgemeinschaft (DFG, German Research Foundation) and the Federal State Government of Saarland (INST 256/298–1 FUGG).

## Declarations

**Conflict of interest** The authors declare that they have no conflict of interest.

**Supplementary Information:** The online version contains supplementary material available at <http://doi.org/10.1007/s10853-022-07398-z>.

**Open Access** This article is licensed under a Creative Commons Attribution 4.0 International License, which permits use, sharing, adaptation, distribution and reproduction in any medium or format, as long as you give appropriate credit to the original author(s) and the source, provide a link to the Creative Commons licence, and indicate if changes were made. The images or other third party material in this article are included in the article's Creative Commons licence, unless indicated otherwise in a credit line to the material. If material is not included in the article's Creative Commons licence and your intended use is not permitted by statutory regulation or exceeds the permitted use, you will need to obtain permission directly from the copyright holder. To view a copy of this licence, visit <http://creativecommons.org/licenses/by/4.0/>.

## References

- [1] Gladman T (1997) The physical metallurgy of microalloyed steels. *Inst Mater*
- [2] Timokhina I, Miller MK, Wang J, Beladi H, Cizek P, Hodgson PD (2016) On the Ti-Mo-Fe-C atomic clustering during interphase precipitation in the Ti-Mo steel studied by advanced microscopic techniques. *Mater Des* 111:222–229. <https://doi.org/10.1016/j.matdes.2016.08.086>
- [3] Misra RDK, Jia Z, O'Malley R, Jansto SJ (2011) Precipitation behavior during thin slab thermomechanical processing and isothermal aging of copper-bearing niobium-microalloyed high strength structural steels: the effect on mechanical properties. *Mater Sci Eng A* 528:8772–8780. <https://doi.org/10.1016/j.msea.2011.08.047>
- [4] Kapoor M, O'Malley R, Thompson GB (2016) Atom probe tomography study of multi-microalloyed carbide and carbonitride precipitates and the precipitation sequence in Nb-Ti HSLA steels. *Metall Mater Trans A* 47:1984–1995. <https://doi.org/10.1007/s11661-016-3398-6>
- [5] Dhara S, Marceau R, Wood K, Dorin T, Timokhina I, Hodgson P (2018) Precipitation and clustering in a Ti-Mo steel investigated using atom probe tomography and small-angle neutron scattering. *Mater Sci Eng A* 718:74–86. <https://doi.org/10.1016/j.msea.2018.01.070>
- [6] Wang H, Somsen C, Li Y, Fries S, Detemple E, Eggeler G (2019) Effect of Nb on improving the impact toughness of Mo-containing low-alloyed steels. *J Mater Sci* 54:7307–7321. <https://doi.org/10.1007/s10853-019-03374-2>
- [7] Pereloma EV, Kostryzhev AG, Alshahrani A, Zhu C, Cairney JM (2014) Effect of austenite deformation temperature on Nb clustering and precipitation in microalloyed steel. *Scr Mater* 75:74–77. <https://doi.org/10.1016/j.scriptamat.2013.11.026>
- [8] Shen YF, Wang CM, Sun X (2011) A micro-alloyed ferritic steel strengthened by nanoscale precipitates. *Mater Sci Eng A* 528:8150–8156. <https://doi.org/10.1016/j.msea.2011.07.065>
- [9] Dong H, Chen H, Wang W, Zhang Y, Miyamoto G, Furuhashi T, Zhang C, Yang Z, van der Zwaag S (2018) Analysis of the interaction between moving  $\alpha/\gamma$  interfaces and interphase precipitated carbides during cyclic phase transformations in a Nb-containing Fe-C-Mn alloy. *Acta Mater* 158:167–179. <https://doi.org/10.1016/j.actamat.2018.07.052>
- [10] Takahashi J, Kawakami K, Tarui T (2012) Direct observation of hydrogen-trapping sites in vanadium carbide precipitation steel by atom probe tomography. *Scr Mater* 67:213–216. <https://doi.org/10.1016/j.scriptamat.2012.04.022>
- [11] Smith E, Nutting J (1956) Direct carbon replicas from metal surfaces. *Br J Appl Phys* 7:214–217. <https://doi.org/10.1088/0508-3443/7/6/304>
- [12] Craven AJ, He K, Garvie LAJ, Baker TN (2000) Complex heterogeneous precipitations in titanium-niobium microalloyed Al-killed HSLA steels – I. (Ti, Nb)(C, N) particles. *Acta Mater* 48:3857–3868. [https://doi.org/10.1016/S1359-6454\(00\)00194-4](https://doi.org/10.1016/S1359-6454(00)00194-4)
- [13] Craven AJ, He K, Garvie LAJ, Baker TN (2000) Complex heterogeneous precipitations in titanium-niobium microalloyed Al-killed HSLA steels – II. Non-titanium based particles. *Acta Materialia* 48:3869–3878. [https://doi.org/10.1016/S1359-6454\(00\)00193-2](https://doi.org/10.1016/S1359-6454(00)00193-2)
- [14] Béreš M, Weirich T, Hulka K, Mayer J (2004) TEM investigations of fine niobium precipitates in HSLA steel. *Steel Res Int* 75:753–758. <https://doi.org/10.1002/srin.200405838>
- [15] Scott C, Chaleix D, Barges P, Rebischung V (2002) Quantitative analysis of complex carbo-nitride precipitates in steels. *Scr Mater* 47:845–849. [https://doi.org/10.1016/S1359-6462\(02\)00219-1](https://doi.org/10.1016/S1359-6462(02)00219-1)
- [16] Charleux M, Poole WJ, Militzer M, Deschamps A (2001) Precipitation behavior and its effect on strengthening of an HSLA-Nb/Ti steel. *Metall Mater Trans A* 32:1635–1647. <https://doi.org/10.1007/s11661-001-0142-6>
- [17] Gong P, Palmiere EJ, Rainforth WM (2015) Dissolution and precipitation behaviour in steels microalloyed with niobium during thermomechanical processing. *Acta Mater* 97:392–403. <https://doi.org/10.1016/j.actamat.2015.06.057>
- [18] Hansen SS, Vander Sande JB, Cohen M (1980) Niobium carbonitride precipitation and austenite recrystallisation in hot-rolled microalloyed steels. *Metall Mater Trans A* 11:387–402. <https://doi.org/10.1007/BF02654563>

- [19] Pavlina EJ, Van Tyne CJ, Speer JG (2015) Effects of combined silicon and molybdenum alloying on the size and evolution of microalloy precipitates in HSLA steels containing niobium and titanium. *Mater Charact* 102:35–46. <https://doi.org/10.1016/j.matchar.2015.02.013>
- [20] Hegetschweiler A, Borovinskaya O, Staudt T, Kraus T (2019) Single-particle mass spectrometry of titanium and niobium carbonitride precipitates in steels. *Anal Chem* 91:943–950. <https://doi.org/10.1021/acs.analchem.8b04012>
- [21] Lu J, Wiskel JB, Omotoso O, Henein H, Ivey DG (2011) Matrix dissolution techniques applied to extract and quantify precipitates from a microalloyed steel. *Metall Mater Trans A* 42:1767–1784. <https://doi.org/10.1007/s11661-010-0579-6>
- [22] Klinkenberg C, Klein H (2016) Synchrotron investigation on the precipitation behaviour of niobium microalloyed steel. *Mater Sci Forum* 879:948–953. <https://doi.org/10.4028/www.scientific.net/msf.879.948>
- [23] Perrard F, Deschamps A, Bley F, Donnadiou P, Maugis P (2006) A small-angle neutron scattering study of fine-scale NbC precipitation kinetics in the  $\alpha$ -Fe-Nb-C system. *J Appl Crystallogr* 39:473–482. <https://doi.org/10.1107/S002188980601301X>
- [24] Shrestha SL, Xie KY, Zhu C, Ringer SP, Killmore C, Carpenter K, Kaul H, Williams JG, Cairney JM (2013) Cluster strengthening of Nb-microalloyed ultra-thin cast strip steels produced by the CASTRIP® process. *Mater Sci Eng A* 568:88–95. <https://doi.org/10.1016/j.msea.2013.01.021>
- [25] Takahashi J, Kawakami K, Kobayashi Y (2012) Consideration of particle-strengthening mechanism of copper-precipitation-strengthened steels by atom probe tomography analysis. *Mater Sci Eng A* 535:144–152. <https://doi.org/10.1016/j.msea.2011.12.056>
- [26] Xie KY, Zheng T, Cairney JM, Kaul H, Williams JG, Barbaro FJ, Killmore CR, Ringer SP (2012) Strengthening from Nb-rich clusters in a Nb-microalloyed steel. *Ser Mater* 66:710–713. <https://doi.org/10.1016/j.scriptamat.2012.01.029>
- [27] Webel J, Herges A, Britz D, Detemple E, Flaxa V, Mohrbacher H, Mücklich F (2020) Tracing microalloy precipitation in Nb-Ti HSLA steel during austenite conditioning. *Metals* 10:243. <https://doi.org/10.3390/met10020243>
- [28] Breen AJ, Xie KY, Moody MP, Gault B, Yen H-W, Wong CC, Cairney JM, Ringer SP (2014) Resolving the morphology of niobium carbonitride nano-precipitates in steel using atom probe tomography. *Microsc Microanal* 20:1100–1110. <https://doi.org/10.1017/S1431927614012872>
- [29] Gault B, Moody MP, Cairney JM, Ringer SP (2012) Atom probe crystallography. *Mater Today* 15:378–386. [https://doi.org/10.1016/S1369-7021\(12\)70164-5](https://doi.org/10.1016/S1369-7021(12)70164-5)
- [30] Hegetschweiler A, Staudt T, Kraus T (2019) An improved method for the matrix dissolution extraction of nanoparticles from microalloyed steel. *J Mater Sci* 54:5813–5824. <https://doi.org/10.1007/s10853-018-03263-0>
- [31] Lees EE, Gunzburg MJ, Nguyen T-L, Howlett GJ, Rothacker J, Nice EC, Clayton AHA, Mulvaney P (2008) Experimental determination of quantum dot size distributions, ligand packing densities, and bioconjugation using analytical ultracentrifugation. *Nano Lett* 8:2883–2890. <https://doi.org/10.1021/nl801629f>
- [32] Schindler T, Walter J, Peukert W, Segets D, Unruh T (2015) In situ study on the evolution of multimodal particle size distributions of ZnO quantum dots: some general rules for the occurrence of multimodalities. *J Phys Chem B* 119:15370–15380. <https://doi.org/10.1021/acs.jpcc.5b08005>
- [33] Schneider CM, Cölfen H (2019) High-resolution analysis of small silver clusters by analytical ultracentrifugation. *J Phys Chem Lett* 10:6558–6564. <https://doi.org/10.1021/acs.jpclett.9b02755>
- [34] Lechner MD (2005) Influence of Mie scattering on nanoparticles with different particle sizes and shapes: photometry and analytical ultracentrifugation with absorption optics. *J Serb Chem Soc* 70:361–369. <https://doi.org/10.2298/JSC0503361L>
- [35] Planken KL, Cölfen H (2010) Analytical ultracentrifugation of colloids. *Nanoscale* 2:1849–1869. <https://doi.org/10.1039/C0NR00215A>
- [36] Okamoto R, Borgenstam A, Ågren J (2010) Interphase precipitation in niobium-microalloyed steels. *Acta Mater* 58:4783–4790. <https://doi.org/10.1016/j.actamat.2010.05.014>
- [37] Kunze J, Mickel C, Backmann G, Beyer B, Reibold M, Klinkenberg C (1997) Precipitation of titanium nitride in low-alloyed steel during cooling and deformation. *Steel Res Int* 68:441–449. <https://doi.org/10.1002/srin.199700580>
- [38] Vurpillot F, Bostel A, Blavette D (2000) Trajectory overlaps and local magnification in three-dimensional atom probe. *Appl Phys Lett* 76:3127. <https://doi.org/10.1063/1.126545>
- [39] Larson DJ, Prosa TJ, Ulfing RM, Geiser BP, Kelly TF (2013) Local electrode atom probe tomography. Springer, New York. <https://doi.org/10.1007/978-1-4614-8721-0>
- [40] Cölfen H, Laue TM, Wohlleben W, Schilling K, Karabudak E, Langhorst BW, Brookes E, Dubbs B, Zollars D, Rocco M, Demeler B (2010) The open AUC project. *Eur Biophys J* 39:347–359. <https://doi.org/10.1007/s00249-009-0438-9>
- [41] Walter J, Peukert W (2016) Dynamic range multiwavelength particle characterization using analytical ultracentrifugation. *Nanoscale* 8:7484–7495. <https://doi.org/10.1039/C5NR08547K>

- [42] Walter J, Löhr K, Karbudak E, Reis W, Mikhael J, Peukert W, Wohlleben W, Cölfen H (2014) Multidimensional analysis of nanoparticles with highly disperse properties using multiwavelength analytical ultracentrifugation. *ACS Nano* 8:8871–8886. <https://doi.org/10.1021/nn503205k>
- [43] Mätzler C (2002) MATLAB functions for Mie scattering and absorption. Institute of Applied Physics, University of Bern. doi: <https://doi.org/10.7892/boris.146550>
- [44] Bohren CF (1983) Huffman, D.R. Absorption and scattering of light by small particles. Wiley. ISBN-13: 978-0-471-29340-8
- [45] Hegetschweiler A (2018) Colloidal analysis of particles extracted from microalloyed steels. PhD thesis, Saarland University, Germany, <https://doi.org/10.22028/D291-27597>
- [46] Thompson K, Lawrence D, Larson DJ, Olson JD, Kelly TF, Gorman B (2007) In situ site-specific specimen preparation for atom probe tomography. *Ultramicroscopy* 107:131–139. <https://doi.org/10.1016/j.ultramic.2006.06.008>
- [47] ASTM E112–10 (2010) Standard test methods for determining average grain size, ASTM International, doi: <https://doi.org/10.1520/E0112-10>
- [48] Cölfen H, Pauck T (1997) Determination of particle size distributions with angström resolution. *Colloid Polym Sci* 275:175–180. <https://doi.org/10.1007/s003960050068>
- [49] Deardo AJ (2003) Niobium in modern steels. *Int Mater Rev* 48:371–402. <https://doi.org/10.1179/095066003225008833>
- [50] Tirumalasetty GK, Van Huis M, Fang C, Xu Q, Tichelaar F, Hanlon D, Sietsma J, Zandbergen H (2011) Characterization of NbC and (Nb, Ti)N nanoprecipitates in TRIP assisted multiphase steels. *Acta Mater* 59:7406–7415. <https://doi.org/10.1016/j.actamat.2011.08.012>
- [51] Roy S, Patra S, Neogy S, Laik A, Choudhary SK, Chakrabarti D (2012) Prediction of inhomogeneous distribution of microalloy precipitates in continuous-cast high-strength, low-alloy steel slab. *Metall Mater Trans A* 43:1845–1860. <https://doi.org/10.1007/s11661-011-1045-9>
- [52] Li YJ, Ponge D, Choi P, Raabe D (2015) Atomic scale investigation of non-equilibrium segregation of boron in a quenched Mo-free martensitic steel. *Ultramicroscopy* 159:240–247. <https://doi.org/10.1016/j.ultramic.2015.03.009>
- [53] Sellars CM (1998) Modelling strain induced precipitation of niobium carbonitride during hot rolling of microalloyed steel. *Mater Sci Forum* 284:73–82. <https://doi.org/10.4028/www.scientific.net/MSF.284-286.73>
- [54] Weibel J, Weber L, Vardo E, Britz D, Kraus T, Mücklich F (2021) Particle encapsulation techniques for atom probe tomography of precipitates in microalloyed steels. *Ultramicroscopy* 223:113219. <https://doi.org/10.1016/j.ultramic.2021.113219>
- [55] Tingaud D, Maugis P (2010) First-principles study of the stability of NbC and NbN precipitates under coherency strains in  $\alpha$ -iron. *Comput Mater Sci* 49:60–63. <https://doi.org/10.1016/j.commatsci.2010.04.020>

**Publisher's Note** Springer Nature remains neutral with regard to jurisdictional claims in published maps and institutional affiliations.